Chemistry–A European Journal | Research Article
doi.org/10.1002/chem.202202966
Chemistry Europe
European Chemical Societies Publishing
www.chemeurj.org

Magnetic Anisotropy and Relaxation of Pseudotetrahedral $[N_2O_2]$ Bis-Chelate Cobalt(II) Single-Ion Magnets Controlled by Dihedral Twist Through Solvomorphism

Maximilian H. Pohle,[a] Michael Böhme,[a] Thomas Lohmiller,[b, c] Sven Ziegenbalg,[a] Louis Blechschmidt,[a] Helmar Görls,[a] Alexander Schnegg,[b, d] and Winfried Plass*[a]

Abstract: The methanol solvomorph **1**·2MeOH of the cobalt(II) complex $[Co(L^{Sal,2-Ph})_2]$ (**1**) with the sterically demanding Schiff-base ligand 2-(([1,1′-biphenyl]-2-ylimino)methyl)phenol ($HL^{Sal,2-Ph}$) shows the thus far largest dihedral twist distortion between the two chelate planes compared to an ideal pseudotetrahedral arrangement. The cobalt(II) ion in **1**·2MeOH exhibits an easy-axis anisotropy leading to a spin-reversal barrier of 55.3 cm^{-1}, which corresponds to an increase of about 17% induced by the larger dihedral twist compared to the solvent-free complex **1**. The magnetic relaxation for **1**·2MeOH is significantly slower compared to **1**. An in-depth frequency-domain Fourier-transform (FD-FT) THz-EPR study not only allowed the direct measurement of the magnetic transition between the two lowest Kramers doublets for the cobalt(II) complexes, but also revealed the presence of spin-phonon coupling. Interestingly, a similar dihedral twist correlation is also observed for a second pair of cobalt(II)-based solvomorphs, which could be benchmarked by FD-FT THz-EPR.

Introduction

Within the class of single-ion magnets (SIMs) derived from transition metals, the cobalt(II)-based examples have been of particular interest due to the large intrinsic magnetic anisotropy of the cobalt(II) ion.[1] In the past, numerous reports have been published on cobalt(II)-based SIMs with a broad range of coordination numbers and geometries,[2] among which the first reported examples are a tetrahedral and a pseudotetrahedral complex with an S_4[3] and N_2O_2[4] coordination sphere at the cobalt(II) ion, respectively. In the case of four-coordinate cobalt(II) SIMs, different magneto-structural correlations for the variation of the magnetic anisotropy have been reported.[5] For tetrahedral $[Co(EPh)_4]^{2-}$ (E = O, S, and Se) complexes, the magnetic anisotropy was found to increase with the softness of the donor atoms and to be sensitive to structural changes even while retaining a fourfold improper rotation axis,[6] whereas for pseudotetrahedral complexes with bis-chelate coordination a decreasing bite angle and an increasing overall charge on the donor atoms is reported to lead to a larger magnetic anisotropy.[7,8] In addition, for bis-chelate complexes also the distortion of the coordination sphere by dihedral twist of two chelate planes is found to be a source of increasing magnetic anisotropy.[8–10]

Here, we report the unique case of two pairs of bis-chelate cobalt(II) SIMs for which the only difference is a variation in the dihedral twist angle between the chelate planes, which is solely induced by the presence or absence of co-crystallized solvent molecules. We present in-depth THz-EPR studies for **1**·2MeOH as well as for another pair of solvomorphs based on the ligand 2-(([1,1′-biphenyl]-2-ylimino)methyl)naphthol ($HL^{Nph,2-Ph}$).

Results and Discussion

The reaction of the bulky Schiff-base ligand 2-(([1,1′-biphenyl]-2-ylimino)methyl)phenol ($HL^{Sal,2-Ph}$) with cobalt(II) acetate in a mixture of methanol and dichloromethane leads to the bis-chelate cobalt(II) complex $[Co(L^{Sal,2-Ph})_2]$ (**1**), which was isolated as crystalline solvent adduct with two co-crystallized molecules of methanol $[Co(L^{Sal,2-Ph})_2]\cdot 2\,CH_3OH$ (**1**·2MeOH) (see Supporting

[a] M. H. Pohle, Dr. M. Böhme, Dr. S. Ziegenbalg, L. Blechschmidt, Dr. H. Görls, Prof. Dr. W. Plass
Institut für Anorganische und Analytische Chemie
Friedrich-Schiller-Universität Jena
Humboldtstraße 8, 07743 Jena (Germany)
E-mail: sekr.plass@uni-jena.de
[b] Dr. T. Lohmiller, Dr. A. Schnegg
EPR4Energy Joint Lab
Department Spins in Energy Conversion and Quantum Information Science
Helmholtz-Zentrum Berlin für Materialien und Energie GmbH
Albert-Einstein-Str. 16, 12489 Berlin (Germany)
[c] Dr. T. Lohmiller
present address: Institut für Chemie
Humboldt-Universität zu Berlin
Brook-Taylor-Str. 2, 12489 Berlin (Germany)
[d] Dr. A. Schnegg
EPR Research Group
MPI for Chemical Energy Conversion
Stiftstr. 34–36, 45470 Mülheim an der Ruhr (Germany)

Supporting information for this article is available on the WWW under https://doi.org/10.1002/chem.202202966

Information). We present in-depth THz-EPR studies for **1**·2MeOH as well as for another pair of solvomorphs based on the ligand 2-(([1,1′-biphenyl]-2-ylimino)methyl)naphthol ($HL^{Nph,2-Ph}$).

The molecular structure of **1**·2MeOH together with the two hydrogen bonded methanol molecules is depicted in Figure 1 (for details see Supporting Information and Table S1). X-ray powder diffraction (XRPD) confirmed the phase purity of **1**·2MeOH and the absence of **1** in the powdered samples used for further characterization (Figure S1). Interestingly, the crystals of the methanol adduct **1**·2MeOH lose the co-crystallized methanol molecules over time, affording the previously reported solvent-free complex **1**[9] in a single-crystal-to-single-crystal transformation, which can be followed by X-ray powder diffraction (XRPD) as depicted in Figure S2. This transformation is irreversible and has been observed to depend on the size distribution of the crystalline material, with larger crystals being more stable over an extended period of several days, even under reduced pressure. In this context, it should also be noted that samples of **1**·2MeOH prepared as pressed pellets from a ground mixture with high-density polyethylene and used for frequency-domain Fourier-transform (FD-FT) THz-EPR measurements[11] exhibit no signs of transformation over several weeks.

The cobalt(II) complexes of **1** and **1**·2MeOH possess the same basic molecular structure with two chelate ligands resulting in a distorted pseudotetrahedral N_2O_2 coordination environment with similar bond lengths and angles (Table S2). However, an essential difference in the molecular structure between the two complexes is found for the dihedral twist angle δ (Figure 1) between the two chelate planes (**1**: 72.5°; **1**·2MeOH: 55.9°). Interestingly, to the best of our knowledge, **1**·2MeOH exhibits the currently largest known deviation from an ideal tetrahedral arrangement (with $\delta = 90°$) for cobalt(II) complexes. This distortion can be further characterized by continuous shape measures (CShM),[12] which clearly show the larger deviation from an ideal tetrahedral arrangement in the case of **1**·2MeOH with a fractional distortion $\phi(T_d \rightarrow D_{4h}) = 43.4$ (tetrahedral: $\phi = 0$, square planar: $\phi = 100$) at a deviation from the ideal path of $\delta_{CShM} = 1.1\,\%$ (Table S3). Consequently, differences in the molecular properties can essentially be attributed to the significant change in the dihedral twist angle, which in turn is due to the presence of the co-crystallized methanol molecules in **1**·2MeOH.

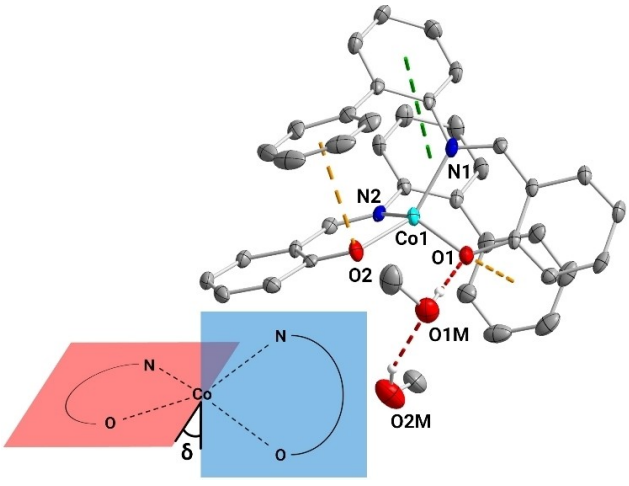

Figure 1. Molecular structure of **1**·2MeOH. Thermal ellipsoids are drawn at the 50% probability level. Hydrogen atoms, except for those in hydrogen bonds (red dashed lines), are omitted for clarity. Intramolecular π-π (green) and lone pair-π (orange) interactions are depicted as dashed lines. The inset illustrates the definition of the dihedral twist angle δ between the chelate planes defined by the cobalt ion and the donor atoms of the individual chelate rings.

The molecular structure of both complexes **1** and **1**·2MeOH is additionally influenced by intramolecular lone pair···π interactions between the phenolate oxygen donors and the terminal phenyl rings of the respective other ligand, resulting in an additional π···π interaction between the central phenyl rings of both ligands (Figure S3 and Table S4). Thus, the basic distortion of the cobalt(II) coordination sphere from an ideal tetrahedral arrangement for both complexes is predefined by these intramolecular interactions. In the case of **1**·2MeOH, the presence of additional intermolecular interactions, including the hydrogen bonding relay with the two methanol molecules (Figure 1), leads to further distortion of the molecular structure, which is associated with a significant decrease of the dihedral twist angle. Additional intermolecular C–H···π interactions are observed for **1**·2MeOH, which are absent in the case of the solvent-free complex **1** (Figures S4–S6 and Table S4).

Magnetic susceptibility data for **1**·2MeOH were collected at an applied static field of 0.1 T between 2 and 250 K (Figure S7) and reveal a $\chi_M T$ value at 250 K of 2.30 $cm^3\,K\,mol^{-1}$, which is considerably higher than the spin-only value ($S = 3/2$: 1.875 $cm^3\,K\,mol^{-1}$), indicative for a strong spin-orbit coupling being present. Below 70 K, a sharp decrease of $\chi_M T$ toward a value of 1.64 $cm^3\,K\,mol^{-1}$ at 2 K is observed, which can be attributed to a large magnetic anisotropy rather than intermolecular spin-spin interactions, since large Co···Co distances are found in **1**·2MeOH (shortest Co1···Co1 distance: 912 pm). The strong magnetic anisotropy is further supported by magnetization measurements at different temperatures (Figure S8), which show that saturation is not reached for fields up to 5 T. The magnetic data were fitted using the spin Hamiltonian given in Equation (1), where the first term represents the Zeeman interaction and the remaining parts the zero-field splitting (ZFS) with the axial and rhombic ZFS parameters D and E, respectively.

$$\hat{H} = g\mu_B B\hat{S} + D\left[\hat{S}_z^{\,2} - \frac{1}{3}S(S+1)\right] + E\left(\hat{S}_x - \hat{S}_y\right) \quad (1)$$

To avoid overparameterization,[13] the ZFS parameters D and E were fixed at the values obtained from the FD-FT THz-EPR and X-band EPR experiments ($D = -26.8\ cm^{-1}$, $E = 3.8\ cm^{-1}$, see below). The best fit results in anisotropic g values of $g_x = 1.98$, $g_y = 2.2$ and $g_z = 2.42$ (Figures S7–S8), which are similar to those obtained for the solvent-free complex **1** ($g_\perp = 2.15$ and $g_\parallel = 2.40$).[9]

For a more detailed insight into the electronic structure of the two solvomorphs, theoretical studies were performed at the CASSCF/CASPT2/RASSI-SO level for DFT-optimized structures (see Table S5 and Figure S9). The ab initio calculations reveal for both complexes a high-spin $^4A_2[^4F]$ ground state multiplet, which splits into two Kramers doublets (KDs) through ZFS (Tables S6-S7). The expected spin-reversal barrier U_{eff} for a single $S=3/2$ spin is taken as the energy difference between the ground state and the first excited KD, which in case of tetrahedrally coordinated cobalt(II) ions is related to the ZFS ($U_{eff} = 2\sqrt{D^2 + 3E^2}$). The calculated ZFS parameters for **1**·2MeOH ($D=-27.7$ cm^{-1}, $E=4.0$ cm^{-1}) reveal an easy-axis anisotropy ($D<0$) with a slight rhombic distortion ($S_{eff}=3/2$, Table S8), and the easy axis of magnetization is found to bisect the N–Co–O bite angles of the two Schiff-base ligands (Figure S10). This results in a calculated barrier U_{eff} of 57.0 cm^{-1}, which is 5 cm^{-1} larger than for **1**. A decomposition of the $^4A_2[^4F]$ ground state (Table S9) for both complexes shows a mixing of different $|S=3/2, m_S>$ eigenfunctions in both KDs, which can be a basis for quantum tunneling of magnetization (QTM) as a possible relaxation pathway when no external static magnetic field is present. Moreover, the corresponding Cartesian g factors for an effective spin $S_{eff}=1/2$, given in Table S10, show a slightly higher g_z factor in the ground state KD of **1**·2MeOH (7.375) compared to **1** (7.302). The magnetic axes for **1**·2MeOH are visualized in Figures S11–S12.

The dynamic magnetic behavior of **1**·2MeOH was studied by alternating-current (ac) susceptibility measurements in the temperature range of 2 to 8 K with an applied static magnetic field (40 and 100 mT) in the frequency range of 10 to 1488 Hz (Figures S13–S16 and Tables S11–S12). Similar to **1**, frequency and temperature dependent maxima in the out-of-phase susceptibility were only observed when an additional static magnetic field was applied, indicating efficient QTM in both complexes. The temperature dependence of the experimental relaxation times τ_c for **1**·2MeOH with an applied static magnetic field of 40 mT is depicted in Figure 2 (for 100 mT see Figure S18).

At low temperatures, the relaxation times for both static fields approach a temperature-independent behavior, supporting the idea of an efficient QTM. In this context, higher applied magnetic fields enlarge the Zeeman splitting and reduce the QTM, thus leading to larger relaxations times for higher dc fields (τ_c(40 mT, $T\rightarrow$2 K)=0.011 s; τ_c(100 mT, $T\rightarrow$2 K)=0.034 s). At temperatures above 5 K, the predominant process is the relaxation via the first excited KD with an exponential dependence according to Equation (2), commonly referred to as the Orbach process. To avoid overparameterization and to address the problem that the spin-reversal barrier U_{eff} is not well defined due to the lack of relaxation data at higher temperatures, this parameter was fixed to the experimental ZFS energy obtained from FD-FT THz-EPR measurements ($U_{THz}=55.3$ cm^{-1}, see below). In addition to these two processes, the relaxation of magnetization could also occur via the coupling with phonon modes with energies below the spin reversal barrier. In the literature, this relaxation is referred to as the Raman process and is commonly parametrized with a power law. Initial fitting

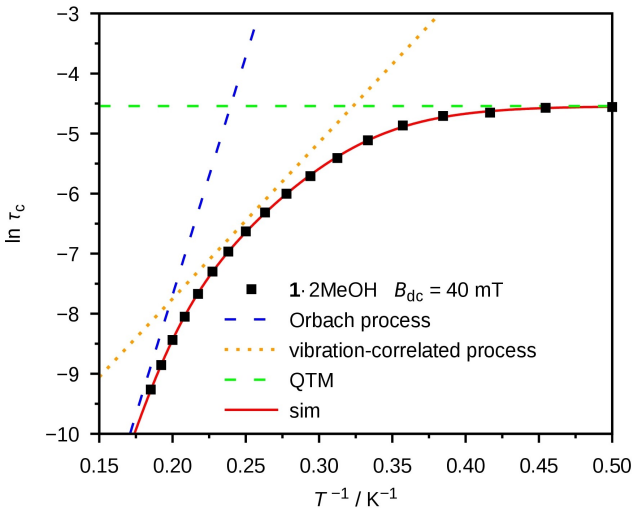

Figure 2. Arrhenius plot of relaxation times for **1**·2MeOH obtained by ac susceptibility measurements (dc field: 40 mT). The best fit to Equation (2) with fixed $U_{THz}=55.3$ cm^{-1} is shown as red solid line. Contributions from specific relaxation processes are included as colored lines (for parameters see Table S13).

of the data using the power law in Equation (S2 in Supporting Information) leads to exponents n of 7.07 and 7.74 for the measurement at 40 and 100 mT, respectively (Figure S17), but this differs from the expected exponents for Kramers systems ($n=9$).[14]

For molecular systems, the description of Raman processes by an exponential term is more suitable than by the conventional power law derived for solid lattices.[15] This allows for a chemical interpretation of the derived parameters of the exponential term as spin-phonon coupling with specific optical phonons (i.e., molecular vibrational modes) with correct symmetry and a strong coupling coefficients with the metal-centered spin.[16] However, in order to keep the number of fit parameters reasonably small, not every single phonon mode can be included with its own exponential term. A more appropriate approach is to use an averaged energy for the underbarrier optical phonons, denoted as U_{vib}, and a single preexponential factor τ_{vib}, which can be interpreted as the corresponding relaxation time. These considerations result in the final fitting Equation (2).

$$\tau_c^{-1} = \tau_0^{-1}\exp\left(\frac{-U_{THz}}{k_B T}\right) + \tau_{vib}^{-1}\exp\left(\frac{-U_{vib}}{k_B T}\right) + QTM \qquad (2)$$

The fit of the relaxation data of **1**·2MeOH using Equation (2) for an applied static magnetic field of 40 mT is given in Figure 2 (see Table S13). In addition, Figure 2 also contains a representation of the individual contributions by the different relaxation processes present in **1**·2MeOH, indicating that the Orbach process via the spin-reversal barrier U_{eff} has only a minor contribution within the accessible temperature range up to 8 K. At the same time, this implies that the higher spin-reversal barrier found for **1**·2MeOH compared to **1** is not the direct cause for the differences in the magnetic relaxation observed in

the investigated temperature range at identical experimental conditions (Table S13). Further details on the analysis of the relaxation behavior of **1**·2MeOH and **1**, as well as additional data derived for a static dc field of 100 mT, is summarized in the Supporting Information (Figures S17–S19 and Table S13).

For a direct experimental determination of the spin-reversal barrier, we have utilized magnetic-field division spectra (MDS) obtained from FD-FT THz-EPR measurements, which are a versatile tool to selectively detect transitions with energies from few to several hundred wavenumbers between magnetic-field-dependent levels.[17] The experimental MDS data for **1**·2MeOH along with a temperature division spectrum (TDS) are shown in Figure S22. The MDS data and the corresponding X-band EPR data, together with simulations obtained for the Hamiltonian given in Equation (1), are depicted in Figure 3. The zero-field transition energy, i.e., the position of the peak maximum in the 0.5 T/0 T spectrum, is defined by the ZFS and readily determines U_{THz} to be 55.3 cm^{-1}. With increasing magnetic field, the sublevels and hence the transition energies are split by the Zeeman interaction. Together with the complementary X-Band EPR data, a fit to Equation (1) and thus the precise determination of the *g* tensor components was possible. The best fit results in anisotropic *g* factors that reveal an easy-axis type of anisotropy ($g_z > g_x, g_y$) with a rhombic distortion ($g_x \neq g_y$) for **1**·2MeOH ($g_x = 2.08$; $g_y = 2.30$; $g_z = 2.48$) and agree with the parameters obtained from the magnetic susceptibility data and the ab initio calculations (see above). The ZFS parameters were fitted with a fixed ratio of *E*/*D* taken from the ab initio calculations according to $U_{THz} = 2\sqrt{D^2 + 3E^2}$ and are listed in Table 1. Compared with the results of the FD-FT THz-EPR measurements for **1** ($U_{THz} = 47.3$ cm^{-1}; $D = -23.1$ cm^{-1}; $E = 2.9$ cm^{-1}),[9] the corresponding spin-reversal barrier for **1**·2MeOH is significantly higher ($U_{THz} = 55.3$ cm^{-1}), which is associated with considerably larger absolute ZFS parameters for **1**·2MeOH ($D = -26.8$ cm^{-1}; $E = 3.8$ cm^{-1}). Consequently, the increased spin-reversal barrier in **1**·2MeOH can be directly attributed to the stronger distortion of the pseudotetrahedral N_2O_2 coordination sphere, since both complex molecules have an identical donor environment.

For magnetic fields above 5 T, the MDS begin to deviate from the simulations and from a linear signal shift due to Zeeman splitting. Two vibrational modes at 68.6 and 70.8 cm^{-1} (see TDS in Figure S22) appear to couple with the magnetic transition, which is confirmed by the occurrence of avoided crossings in the overlap-region, as shown in Figure S23. Below approximately 3 T, where the magnetic transitions are sufficiently well separated in energy, the phonons are no longer field dependent and vanish from the spectra in Figure 3, due to the applied field division method. A simulation of this interaction with visually estimated spin-phonon coupling constants is given in the Supporting Information. It is worth noting that this is consistent with the fact that the magnetic relaxation of **1**·2MeOH above 3 K is dominated by a vibration-correlated process.

To corroborate our findings, we additionally performed FD-FT THz-EPR measurements for another pair of cobalt(II)-based complexes with solvomorphism that we previously reported,

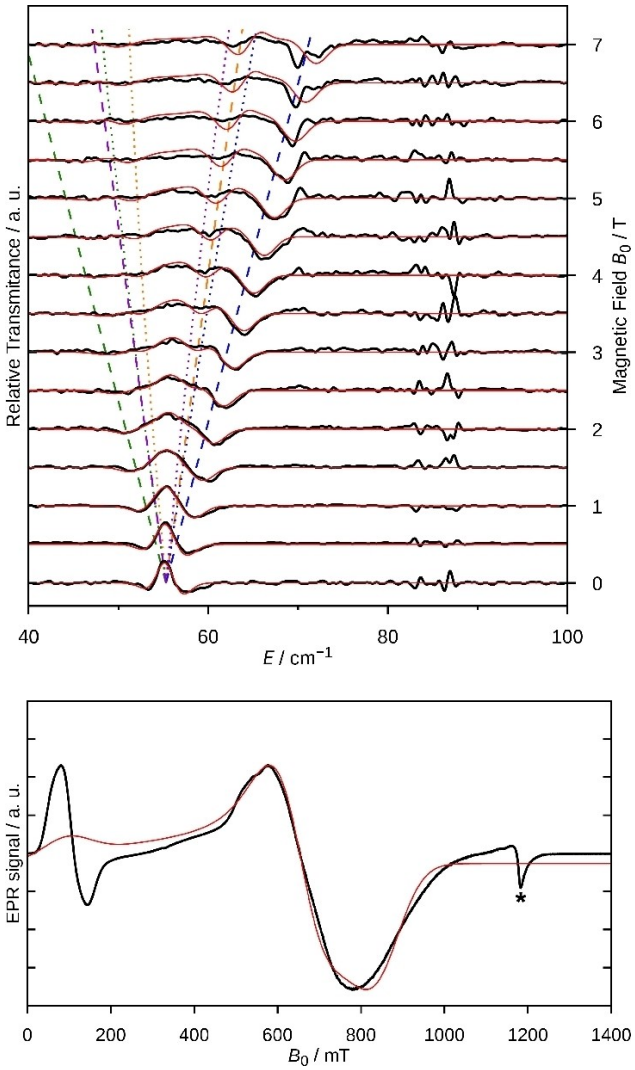

Figure 3. Top: Experimental (black lines) and simulated (red lines) magnetic-field division spectra (MDS) of FD-FT THz-EPR measurements for **1**·2MeOH at 4.6 K. The MDS were obtained by division of raw spectra ($(B_0 + 0.5\ T)/B_0$). Lines represent transition energies between m_S states: −3/2→−1/2 (orange), −3/2→1/2 (blue), 3/2→−1/2 (green), and 3/2→1/2 (purple); $B_0 || z$ (dashed) and $B_0 \perp z$ (dotted). Bottom: Experimental X-band EPR spectrum of **1**·2MeOH at 4.5 K (black line) and simulated (red line). The feature marked with an asterisk is a background signal from the cavity used. Simulations were optimized by simultaneous least-square fitting of the MDS up to 3.5 T/3 T and the X-band spectrum.

Table 1. ZFS parameters obtained by simulations of the FD-FT THz-EPR spectra for **1**, **1**·2MeOH, **2**, and **2**·CH_2Cl_2 with $S_{eff} = 3/2$ and $U_{THz} = 2\sqrt{D^2 + 3E^2}$.

	Δ [°]	D [cm^{-1}]	E [cm^{-1}]	$\lvert E/D \rvert$	U_{THz} [cm^{-1}]	Ref.
1·2MeOH	55.9	−26.8	3.8	0.142	55.3	this work
1	72.5	−23.1	2.9	0.126	47.3	[9]
2	65.3	−30.6	4.1	0.134	62.8	[9]
2·CH_2Cl_2	78.8	−25.1	1.8	0.072	50.6	this work

namely [Co($L^{Nph,2\text{-}Ph}$)$_2$] (**2**)[9] and [Co($L^{Nph,2\text{-}Ph}$)$_2$]·CH_2Cl_2 (**2**·CH_2Cl_2).[8] Like **1** and **1**·2MeOH, these complexes also exhibit a significant difference in their dihedral twist angles δ (**2**: 65.3°; **2**·CH_2Cl_2:

79.0°), but both of them are considerably larger than that observed for **1**·2MeOH. However, in contrast to the methanol molecules in **1**·2MeOH the additional dichloromethane molecule in the crystal structure of **2**·CH_2Cl_2 leads to an increase of δ compared to **2**, that is, to a weaker twist distortion of the N_2O_2 coordination sphere. As expected, this leads to a reduced spin-reversal barrier U_{THz} for **2**·CH_2Cl_2 (50.6 cm^{-1}, Figure 4) compared to **2** (62.8 cm^{-1}),[9] both values determined by FD-FT THz-EPR (see Table 1). This again proves that the spin-reversal barrier is affected by the twist distortion of the coordination sphere induced by co-crystallized molecules, and agrees perfectly with our results for **1**·2MeOH and **1**. It should be noted here that for **2**·CH_2Cl_2 no X-Band EPR signal could be observed, which can be attributed to the reduced dihedral twist distortion that is expected to lead to a considerably smaller rhombic distortion. Details of a complementary analysis of the magnetic relaxation behavior of **2** and **2**·CH_2Cl_2 are summarized in the Supporting Information.

At this point, it is interesting to note that increasing the rhombicity of the ZFS leads to a significantly more pronounced QTM (see Table S13) when comparing **2**·CH_2Cl_2 ($|E/D| = 0.072$) and **1**·2MeOH ($|E/D| = 0.142$). This can be rationalized by a somewhat higher degree of admixing of m_S eigenstates, which is evident for **1**·2MeOH from Table S9.

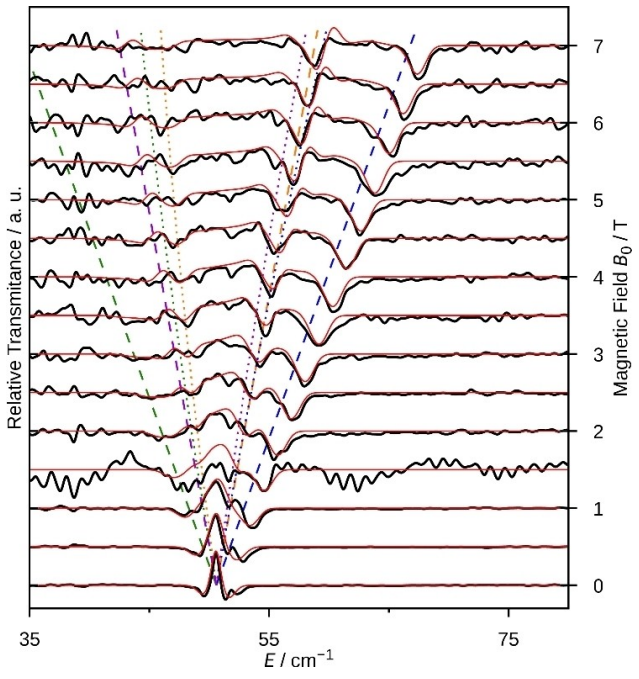

Figure 4. Experimental (black lines) and simulated (red lines) magnetic-field division spectra (MDS) of FD-FT THz-EPR measurements for **2**·CH_2Cl_2 at 4.6 K. The MDS were obtained by division of raw spectra ($(B_0 + 0.5\ T)/B_0$). The simulations were optimized by least-square fitting up to 5.5 T/5 T (with exception of 1.5 T/1 T, which is impaired by an experimental artefact). Lines represent transition energies between m_S states: −3/2→−1/2 (orange), −3/2→1/2 (blue), 3/2→−1/2 (green), and 3/2→1/2 (purple); $B_0 || z$ (dashed) and $B_0 \perp z$ (dotted).

Conclusion

In conclusion, the new solvomorph **1**·2MeOH of a bis-chelate cobalt(II)-based complex is presented, which exhibits the largest currently known dihedral twist distortion between its chelate planes ($\delta = 55.9°$) within the pseudotetrahedral coordination sphere ($\delta = 90°$ for an ideal tetrahedral arrangement). Moreover, it could be demonstrated by FD-FT THz-EPR experiments that U_{eff} for pseudotetrahedral cobalt(II) complexes can be increased by enforcing a stronger distortion of the coordination sphere toward a square-planar geometry, which in the current case of **1**·2MeOH leads to an increase of approximately 17%. These results have been used to benchmark the corroborating ab initio calculations and susceptibility data analysis, which are in good agreement and show an easy-axis type of magnetic anisotropy. Finally, the obtained dataset of complementary experimental and theoretical results allowed for a more detailed view on the magnetic relaxation, which above 3 K was found to be dominated by a vibration-correlated process, consistent with the observed evidence for spin-phonon couplings in **1**·2MeOH.

Experimental Section

Materials and Instrumentation: All reagents were purchased from commercial sources at reagent grade and used without further purification. Solvents were distilled once from CaH_2 prior to use. The bis-chelate ligand 2-(([1,1′-biphenyl]-2-ylimino)methyl)naphthol ($HL^{Nph,2-Ph}$) was prepared as reported in literature.[9] The complexes **1**,[9] **2**,[9] and **2**·CH_2Cl_2[8] were prepared as previously described. IR spectra were measured with a Bruker Equinox spectrometer equipped with a diamond ATR unit. Elemental analyses (C, H, N) were carried out on Leco CHNS-932 and El Vario III elemental analyzers.

Synthesis of $[Co(L^{Sal,2-Ph})_2]\cdot 2CH_3OH$ (1·2MeOH): The ligand $HL^{Sal,2-Ph}$ (410 mg, 1.5 mmol) was dissolved in methanol (8 mL). Under continuous stirring a solution of $[Co(OAc)_2]\cdot 4H_2O$ (201 mg, 0.82 mmol) in CH_2Cl_2 (8 mL) was added. After 5 min of further stirring, the red solution was filtered off and kept sealed at room-temperature. After 4–7 days red-brown crystals could be isolated.

Yield: 17.3% (0.0947 g, 0.142 mmol). Elemental Analysis: Anal. calcd (%) for $C_{40}H_{36}N_2CoO_4$ (667.66 g cm^{-3}): C 71.96, H 5.44, N 4.20. Found (%): C 72.19, H 5.44, N 4.29. IR (ATR, selected bands, cm^{-1}): 3053 (w, υ(C–H)), 3018 (w, υ(C–H)), 1606 (s),1575 (s), 1524 (s), 1438 (vs), 1381 (s), 1329 (s), 1176 (s), 1148 (s), 763 (s), 751 (vs), 736 (vs), 724 (vs), 700 (vs), 533 (s), 506 (s).

Crystal Structure Determination: The intensity data were collected on a Nonius KappaCCD diffractometer, using graphite-monochromated $Mo_{K\alpha}$ radiation. Data were corrected for Lorentz and polarization effects,[18,19] while absorption was taken into account on a semi-empirical basis using multiple-scans (SADABS 2016/2).[20] The structure was solved by direct methods (SHELXT)[21] and refined by full-matrix least squares techniques against F_o^2 (SHELXL-2018).[22] All hydrogen atoms were included at calculated positions with fixed thermal parameters. All non-hydrogen atoms were refined anisotropically (SHELXL-2018).[22] The crystal of **1**·2MeOH was a non-merohedral twin. The twin law was determined by PLATON[23] to (−1 0 0) (0 −1 0) (0.039 0 1). The contribution of the main component was refined to 0.770(3). For crystallographic details see Table S1. Diamond 4.4.1 was used for structure representations.[24]

Deposition Number(s) 2118169 (for **1**·2MeOH) contain(s) the supplementary crystallographic data for this paper. These data are provided free of charge by the joint Cambridge Crystallographic Data Centre and Fachinformationszentrum Karlsruhe Access Structures service.

X-Ray Powder Diffraction (XRPD): X-ray diffraction measurements on powdered samples were performed on a Stoe powder diffractometer with a MYTHEN 1 K detector at room temperature. Measurements were performed using capillary tubes open to air using the Debye Scherrer scan mode with a 2Θ scan type. The X-ray tube was a Cu-long fine focus tube. The measurement was carried out between 2 and 50° with steps of 2.1° per 20 seconds.

Magnetic Measurements: The magnetic data were collected using a Quantum Design MPMS-5 SQUID magnetometer. The sample was prepared from powdered polycrystalline material. To avoid orientation in the magnetic field the material was fixed with paraffin. Susceptibility data were measured at a static field of 0.2 T with a temperature range of 2 to 250 K. Magnetization data were measured at different temperatures between 2 and 5 K for magnetic fields up to 5 T. All data were corrected by subtracting a fitted temperature independent value. Simulations of the data were carried out with the program PHI.[25] Ac susceptibility data was measured with alternating fields of 0.1 mT magnitude and constant dc fields of 40 and 100 mT in the frequency range from 10 to 1488 Hz at temperatures between 2 and 8 K. The frequencies used are: 10, 13, 17, 22, 28.7, 37.3, 55, 63.2, 82.2, 106.9, 139.1, 181, 235.6, 306.4, 398.9, 518, 674.5, 876.2, 1143.3, and 1488.1 Hz. To quench any residual remanence between the measurements, the sample was heated up to 60 K and the field was set to zero in an oscillating approach. After cooling down to the next starting temperature, the new field was applied in a 'no overshoot' approach.

X-Band EPR Spectroscopy: The measurements were performed on a Bruker E580 in an MS-5 resonator at 4.5 K with a microwave frequency of 9.39 GHz. The powdered samples were prepared by grinding single crystals of **1**·2MeOH or **2**·CH_2Cl_2 and filled into EPR tubes.

FD-FT THz-EPR Spectroscopy: Low temperature FD-FT THz-EPR measurements carried out at the THz-EPR experiment of the BESSY II facility at Helmholtz-Zentrum Berlin (HZB) were used to determine magnetic-field dependent transitions between 30 and 100 cm^{-1}. The used spectrometer is described in the literature.[26] Its main components are a high-resolution FTIR spectrometer equipped with a Hg arc lamp as the radiation source, an evacuated quasi-optical transmission line, a 10 T superconducting magnet and a liquid He cooled bolometer detector. Samples were prepared by homogenizing 22 mg of polycrystalline **1**·2MeOH or **2**·CH_2Cl_2 with 43–47 mg polyethylene (PE) powder in a mortar and pressing them into pellets. Spectra were recorded in Voigt geometry with an experimental resolution of 0.5 cm^{-1} for applied fields from 0 to 7.5 T in 0.5 T steps. MDS were obtained by dividing a raw spectrum by a spectrum measured at 0.5 T lower field. The relative transmittance T_{sim} in MDS is calculated from the simulated absorbance spectra A at different fields B as $T_{sim} = 10^{A_{B2} - A_{B1}}$. Prior to fitting, MDS were normalized by division with the absolute value derived from the maximum intensity difference within each spectrum ($|I_{max} - I_{min}|$). Simulation of the normalized MDS together with the X-Band EPR spectrum was performed with the Matlab EPR toolbox EasySpin.[27,28]

Computational Details: The model structures used for the ab initio studies depicted in Figure S9 were obtained by a full DFT optimization of the molecular structures starting from the atomic positions as derived from the single-crystal structure data of **1**·2MeOH and **1**. The position of all atoms was optimized at RI-DFT-D3/BP86/def2-TZVPP level of theory with the Turbomole 7.2 package of programs.[29] Ab initio calculations based on these DFT-optimized structures were performed with the MOLCAS 8.0 SP1 package of programs.[30] For all ab initio calculations ANO-RCC basis sets (see Table S5) have been employed in combination with a scalar-relativistic second-order Douglas–Kroll–Hess Hamiltonian. To speed up calculations, the Cholesky decomposition of integrals was used as implemented in MOLCAS. CASSCF calculations were performed with 7 electrons in 10 orbitals (3d and 4d shell) for 10 quartet (^4F and ^4P) and 40 doublet states (^2G, ^2P, ^2H, ^2D, ^2D, ^2F). Additional dynamic correlation was subsequently treated by CASPT2 on the basis of the optimized CASSCF wave function for all quartet and the 12 lowest doublet states. Corresponding energies are summarized in Table S6. CASSCF/CASPT2/SO-RASSI calculations were carried out to take spin-orbit coupling adequately into account (for energies see Table S7). The SINGLE_ANISO module was employed to obtain magnetic parameters for the effective spin models $S_{eff} = {}^2/_3$ (see Tables S8–S9 and Figure S10) and $S_{eff} = {}^1/_2$ (see Table S10 and Figures S11–S12).

Acknowledgements

We thank Dr. Axel Buchholz and Florian Reinhardt for the measurement of the magnetic data. We are thankful to Dr. Karsten Holldack for his support with the FD-FT THz-EPR measurements. We thank HZB for the allocation of synchrotron radiation beamtime at BESSY II (Plass 192–08790 and 221–10795) and thankfully acknowledge the financial support by HZB. T.L. is indepted to the Deutsche Forschungsgemeinschaft (DFG, LO 2898/1–1). Open Access funding enabled and organized by Projekt DEAL.

Conflict of Interest

There are no conflicts to declare.

Data Availability Statement

The data that support the findings of this study are available in the supplementary material of this article.

Keywords: cobalt · electronic structure · EPR spectroscopy · magnetic anisotropy · single-ion magnets

[1] a) G. A. Craig, M. Murrie, *Chem. Soc. Rev.* **2015**, *44*, 2135–2147; b) J. M. Frost, K. L. M. Harriman, M. Murugesu, *Chem. Sci.* **2016**, *7*, 2470–2491; c) S. Gómez-Coca, D. Aravena, R. Morales, E. Ruiz, *Coord. Chem. Rev.* **2015**, *289–290*, 379–392.
[2] a) S. Tripathi, A. Dey, M. Shanmugam, R. S. Narayanan, V. Chandrasekhar in *Top. Organomet. Chem.* (Eds.: V. Chandrasekhar, F. Pointillart), Springer, Cham, **2019**, pp. 35–75; b) A. Sarkar, S. Dey, G. Rajaraman, *Chem. Eur. J.* **2020**, *26*, 14036–14058; c) P. K. Sahu, R. Kharel, S. Shome, S. Goswami, S. Konar, *Coord. Chem. Rev.* **2023**, *475*, 214871.
[3] J. M. Zadrozny, J. R. Long, *J. Am. Chem. Soc.* **2011**, *133*, 20732–20734.
[4] A. Buchholz, A. O. Eseola, W. Plass, *C. R. Chim.* **2012**, *15*, 929–936.
[5] a) S. Ostrovsky, *Polyhedron* **2021**, *194*, 114936; b) M. Idešicová, J. Titiš, J. Krzystek, R. Boča, *Inorg. Chem.* **2013**, *52*, 9409–9417.

[6] a) J. M. Zadrozny, J. Telser, J. R. Long, *Polyhedron* **2013**, *64*, 209–217; b) E. A. Suturina, D. Maganas, E. Bill, M. Atanasov, F. Neese, *Inorg. Chem.* **2015**, *54*, 9948–9961; c) E. A. Suturina, J. Nehrkorn, J. M. Zadrozny, J. Liu, M. Atanasov, T. Weyhermüller, D. Maganas, S. Hill, A. Schnegg, E. Bill, J. R. Long, F. Neese, *Inorg. Chem.* **2017**, *56*, 3102–3118; d) A. Sarkar, S. Tewary, S. Sinkar, G. Rajaraman, *Chem. Asian J.* **2019**, *14*, 4696–4704.
[7] a) E. Carl, S. Demeshko, F. Meyer, D. Stalke, *Chem. Eur. J.* **2015**, *21*, 10109–10115; b) Y. Rechkemmer, F. D. Breitgoff, M. van der Meer, M. Atanasov, M. Hakl, M. Orlita, P. Neugebauer, F. Neese, B. Sarkar, J. van Slageren, *Nat. Commun.* **2016**, *7*, 10467; c) M. Wang, H.-J. Xu, T.-M. Sun, H.-H. Cui, Y.-Q. Zhang, L. Chen, Y.-F. Tang, *J. Solid State Chem.* **2021**, *299*, 122209.
[8] S. Ziegenbalg, D. Hornig, H. Görls, W. Plass, *Inorg. Chem.* **2016**, *55*, 4047–4058.
[9] a) M. Böhme, S. Ziegenbalg, A. Aliabadi, A. Schnegg, H. Görls, W. Plass, *Dalton Trans.* **2018**, *47*, 10861–10873; b) M. Böhme, S. Ziegenbalg, A. Aliabadi, A. Schnegg, H. Görls, W. Plass, *Dalton Trans.* **2019**, *48*, 11142–11143.
[10] G. Peng, Y. Chen, B. Li, Y.-Q. Zhang, X.-M. Ren, *Dalton Trans.* **2020**, *49*, 5798–5802.
[11] J. Nehrkorn, K. Holldack, R. Bittl, A. Schnegg, *J. Magn. Reson.* **2017**, *280*, 10–19.
[12] a) S. Alvarez, P. Alemany, D. Casanova, J. Cirera, M. Llunell, D. Avnir, *Coord. Chem. Rev.* **2005**, *249*, 1693–1708; b) J. Cirera, P. Alemany, S. Alvarez, *Chem. Eur. J.* **2004**, *10*, 190–207; c) J. Cirera, E. Ruiz, S. Alvarez, *Chem. Eur. J.* **2006**, *12*, 3162–3167.
[13] J. Krzystek, J. Telser, *Dalton Trans.* **2016**, *45*, 16751–16763.
[14] K. N. Shrivastava, *Phys. Status Solidi B* **1983**, *117*, 437–458.
[15] a) L. Gu, R. Wu, *Phys. Rev. B* **2021**, *103*, 014401; b) A. Lunghi, *Sci. Adv.* **2022**, *8*, eabn7880.
[16] N. P. Kazmierczak, R. Mirzoyan, R. G. Hadt, *J. Am. Chem. Soc.* **2021**, *143*, 17305–17315.
[17] a) A. Jochim, T. Lohmiller, M. Rams, M. Böhme, M. Ceglarska, A. Schnegg, W. Plass, C. Näther, *Inorg. Chem.* **2020**, *59*, 8971–8982; b) M. Böhme, A. Jochim, M. Rams, T. Lohmiller, S. Suckert, A. Schnegg, W. Plass, C. Näther, *Inorg. Chem.* **2020**, *59*, 5325–5338; c) M. Rams, A. Jochim, M. Böhme, T. Lohmiller, M. Ceglarska, M. M. Rams, A. Schnegg, W. Plass, C. Näther, *Chem. Eur. J.* **2020**, *26*, 2837–2851.
[18] R. W. W. Hooft, **1998**, COLLECT, Data Collection Software, Nonius BV, Delft, The Netherlands.
[19] Z. Otwinowski, W. Minor, in *Macromolecular Crystallography, Part A* (Eds.: C. W. Carter, R. M. Sweet), *Methods in Enzymology*, Academic Press: San Diego, **1997**; Vol. 276; pp. 307–326.
[20] L. Krause, R. Herbst-Irmer, G. M. Sheldrick, D. Stalke, *J. Appl. Crystallogr.* **2015**, *48*, 3–10.
[21] G. M. Sheldrick, *Acta Crystallogr.* **2015**, *A71*, 3–8.
[22] G. M. Sheldrick, *Acta Crystallogr.* **2015**, *C71*, 3–8.
[23] A. L. Spek, *Acta Crystallogr.* **2015**, *C71*, 9–18.
[24] K. Brandenburg, *Diamond*, Crystal Impact, Bonn, Germany, **2020**.
[25] N. F. Chilton, R. P. Anderson, L. D. Turner, A. Soncini, K. S. Murray, *J. Comput. Chem.* **2013**, *34*, 1164–1175.
[26] a) K. Holldack, A. Schnegg, *J. Large-Scale Res. Facil. JLSRF* **2016**, *2*, A51; b) J. Nehrkorn, K. Holldack, R. Bittl, A. Schnegg, *J. Magn. Reson.* **2017**, *280*, 10–19.
[27] S. Stoll, A. Schweiger, *J. Magn. Reson.* **2006**, *178*, 42–55.
[28] a) J. Nehrkorn, J. Telser, K. Holldack, S. Stoll, A. Schnegg, *J. Phys. Chem. B* **2015**, *119*, 13816–13824; b) J. Nehrkorn, A. Schnegg, K. Holldack, S. Stoll, *Phys. Rev. Lett.* **2015**, *114*, 010801.
[29] a) F. Weigend, R. Ahlrichs, *Phys. Chem. Chem. Phys.* **2005**, *7*, 3297–3305; b) TURBOMOLE V7.2 2017, a development of University of Karlsruhe and Forschungszentrum Karlsruhe GmbH, 1989–2007, TURBOMOLE GmbH, since 2007; available from http://www.turbomole.com.
[30] a) G. Karlström, R. Lindh, P.-Å. Malmqvist, B. O. Roos, U. Ryde, V. Veryazov, P.-O. Widmark, M. Cossi, B. Schimmelpfennig, P. Neogrady, *Comput. Mater. Sci.* **2003**, *28*, 222–239; b) F. Aquilante, L. De Vico, N. Ferré, G. Ghigo, P.-Å. Malmqvist, P. Neogrády, T. B. Pedersen, M. Pitoňák, M. Reiher, B. O. Roos, *J. Comput. Chem.* **2010**, *31*, 224–247; c) F. Aquilante, J. Autschbach, R. K. Carlson, L. F. Chibotaru, M. G. Delcey, L. De Vico, N. Ferré, L. M. Frutos, L. Gagliardi, M. Garavelli, *J. Comput. Chem.* **2016**, *37*, 506–541.

Manuscript received: September 22, 2022
Accepted manuscript online: December 5, 2022
Version of record online: February 3, 2023